Research Article

Journal of Environmental Nanotechnology

Development of Chitosan/TiO_2 Nanocomposite Films Using Banana Flower Spathe Extract for Tissue-Regeneration Applications

Anju Rani[1], Dhananjay Bhaurao Awachat[2], P. Satishkumar[3], Purushottam barve[4], Sandeep Gaikwad[5] and K. Raajananthini[6*]

[1]Department of Physics, School of Engineering and Technology, CGC University, Mohali, PB, India
[2]Department of Civil Engineering, K D K College of Engineering, Nagpur, MH, India
[3]Department of Mechanical Engineering, Rathinam Technical Campus, Coimbatore, TN, India
[4]Department of Mechanical Engineering, Yeshwantrao Chavan College of Engineering, Nagpur, MH, India
[5]Department of Civil Engineering, Tulsiramji Gaikwad Patil College of Engineering and Technology, Nagpur, MH, India
[6]Department of Science and Humanities, Rathinam Technical Campus, Coimbatore, TN, India
Received: 29.07.2026 Accepted: 26.08.2026 Published: xx.xx.xxxx
*raajananthinik@gmail.com

ABSTRACT

Banana flower spathe extract-mediated titanium dioxide nanoparticles (TiO_2 NPs) were incorporated into chitosan to fabricate functional nanocomposite films for tissue-engineering applications. TiO_2 NPs were produced from titanium(IV) isopropoxide (TTIP), and their formation was verified using UV–visible spectroscopy. Chitosan/TiO_2 films containing 5, 10, and 20 mL of nanoparticle suspension were prepared through solution casting. Structural, chemical, and morphological characteristics were investigated using XRD, FTIR, and SEM, respectively. These analyses supported the successful incorporation of TiO_2 and indicated comparatively uniform nanoparticle dispersion in the 10 mL formulation. The films were further examined for tensile performance, antibacterial potential, antioxidant activity, swelling, biodegradation, and titanium release. The formulation containing 10 mL of TiO_2 suspension exhibited the most favourable performance, with tensile strength of 48.9 MPa and electrical conductivity of 6.80×10−7 S cm^{-1}. It demonstrated 4.7% cumulative titanium release after 12 h and 45.08 % antioxidant activity. Controlled swelling confirmed structural stability under hydrated conditions, while gradual biodegradation supported temporary biomedical use. The combined properties justify further cytocompatibility, nanoparticle-migration, and in vivo evaluation of the optimized film for potential tissue-support and wound-contact applications.

Keywords: Green synthesis; Nanocomposite films; Antibacterial activity; UV-vis spectroscopy; Biodegradation.

1. INTRODUCTION

Biodegradable polymeric materials have attracted considerable attention as sustainable alternatives to petroleum-based materials because of their biodegradability, biocompatibility, low toxicity, and excellent film-forming ability. Among these materials, chitosan has emerged as one of the most promising natural polymers for biomedical and packaging applications owing to its intrinsic antimicrobial activity, hydrophilicity, and ability to form multifunctional composites with organic and inorganic nanofillers. Nevertheless, pristine chitosan films generally exhibit limited mechanical strength, moisture resistance, and long-term stability, restricting their practical application. Consequently, recent research has focused on reinforcing chitosan matrices with bioactive compounds, nanomaterials, and plant-derived extracts to simultaneously improve their structural integrity and functional performance.

Recent studies have demonstrated that, the incorporation of natural antioxidants and nanofillers substantially enhances the physicochemical properties of biodegradable films. Chitosan–DES–proanthocyanidin composite films exhibited a tensile strength of 2.63 ± 0.48 MPa, 73.22% elongation, 88.4° water contact angle, and only 5% water swelling, confirming improved barrier performance (Zhou *et al.* 2024). Likewise, chitosan/gelatin films reinforced with 5% broccoli-derived carbon dots achieved a tensile strength of 80.32 MPa, approximately 90% DPPH radical scavenging activity, and only ~13% water solubility, resulting in enhanced UV-shielding and antibacterial performance (Tran *et al.* 2025). Similarly, PVA films reinforced with 15% tannin-cellulose nanocrystals exhibited a tensile strength of 74.17 MPa, 75% DPPH scavenging activity, and 66.7% lower oxygen permeability than neat PVA films (Qin *et al.* 2024). Sericin/pectin films containing 1.6% thyme/oregano essential oil also improved antioxidant activity to 3.68 μmol Trolox g^{-1} while increasing total phenolic content to 31.53 mg GAE g^{-1},

despite reduced tensile strength (Meerasri *et al.* 2024). Moreover, PVA/chitosan bio-nanocomposite films reinforced with 10 wt% cellulose nanocrystals reduced water vapor, carbon dioxide, and oil permeability by 30.95%, 39.22%, and 14.28%, respectively, while increasing tensile strength from 1.25 ± 0.14 to 3.45 ± 0.40 MPa (Yadav *et al.* 2026).

Green synthesis has become an attractive strategy for producing environmentally friendly nanomaterials using plant extracts as reducing and stabilizing agents. Flaxseed extract-mediated CdS nanoparticles incorporated into PVA/chitosan films exhibited characteristic absorption at 396–440 nm, while 20 and 40 kGy gamma irradiation improved nanoparticle dispersion, thermal stability, and antibacterial activity (Sokary *et al.* 2024). Carbon dot-reinforced biodegradable hydrogels also demonstrated controlled biodegradation with <75% weight loss within 3 weeks, together with improved barrier properties and antibacterial performance (Alzahrani, 2024). Similarly, chitosan/PVA films containing 3.0 wt% CeO_2 nanoparticles successfully preserved tomatoes for 25 days while improving antimicrobial and antioxidant properties (Ali *et al.* 2024). Chitosan films embedded with green-synthesized Ag nanoparticles produced by 15–90 min UV photoreduction generated nanoparticles of approximately 60 nm and effectively inhibited *Escherichia coli* and Staphylococcus aureus (Costa *et al.* 2026). Likewise, chitosan/gelatin/PEG films reinforced with green Ag nanoparticles exhibited inhibition zones of 11 mm and 12 mm against *E. coli* and *S. aureus*, respectively, together with 33–46% soil biodegradation (Balapure *et al.* 2026), whereas chitosan/polycaprolactone composites containing 3 wt% Ag nanoparticles produced inhibition zones of 9 mm against *E. coli* and 10 mm against *Candida albicans* (Pekdemir *et al.* 2025).

The incorporation of multifunctional nanomaterials has further expanded the application potential of biodegradable composites beyond conventional packaging. Cotton fabrics coated with green Ag/HG/Ti nanocomposites increased tensile strength from 67.1 to 85.7 N, water contact angle from 0° to 151.3°, and UV protection factor from 2.1 to 45.1, while maintaining >90% antibacterial efficiency after 15 washing cycles (Alfaifi *et al.* 2025). Chitosan-coated Ag/TiO_2 nanocomposites synthesized using Matricaria chamomilla extract exhibited an IC_{50} of 0.769 mg mL^{-1} and inhibition zones of 22 ± 1.17 mm against *S. aureus* (Alzahrani *et al.* 2025). Furthermore, chitosan/collagen-stabilized Ag@TiO_2@ZnO nanocomposites synthesized using curcuminoid extract exhibited particle sizes of 11–52 nm, MIC values of 0.4–0.9 mg mL^{-1}, and 96.17% cell viability, demonstrating their biomedical potential (Emam *et al.* 2026). Green-synthesized silver nanoparticles using banana flower extract also displayed MIC values of 16 µg mL^{-1} against *E. coli* and 32 µg mL^{-1} against *S. aureus* through ROS-mediated antibacterial mechanisms (Weiming *et al.* 2023).

Apart from food packaging, biodegradable polymer composites are increasingly investigated for tissue engineering, wound healing, and environmentally sustainable materials. PHB/corn starch composites with a 70:30 ratio exhibited superior tensile performance and biodegradation behavior (Shankar and Venkatesh 2025), while PLA composites reinforced with carbonized rice husk demonstrated improved mechanical strength, crystallinity, and reduced moisture absorption (Reddy and Venkatachalapathi, 2025). Likewise, sodium alginate/Sida cordifolia hydrogel scaffolds reinforced with green ZnO nanoparticles exhibited a swelling capacity of 5.8 g g^{-1}, 48.7% degradation after 385 h, nanoparticle size of 6.26 nm, and inhibition zones of 16 mm against *S. aureus* and 14 mm against *E. coli*, confirming their suitability for biomedical applications (Subbarayalu *et al.* 2026).

Although previous investigations have demonstrated considerable improvements in the mechanical, antioxidant, and antimicrobial properties of biodegradable polymer composites through various green-synthesized nanomaterials, the combined use of banana flower spathe extract as a plant-derived medium for TiO_2 synthesis and chitosan as a film-forming matrix has received limited systematic investigation. Most previous studies have examined nanoparticles synthesis or individual film properties separately, without concurrently relating TiO_2 incorporation to mechanical, electrical, swelling, degradation, antioxidant, antibacterial, and titanium-release behaviour within a single system. Therefore, the present study aims to synthesize TiO_2 nanoparticles using banana flower spathe extract through an eco-friendly route and incorporate them into chitosan films via solution casting. The specific novelty lies in comparatively evaluating films containing 5, 10, and 20 mL of TiO_2 suspension to identify a formulation with balanced structural, physicochemical, and functional properties. Rather than confirming biomedical suitability, the study provides preliminary evidence supporting further cytocompatibility, nanoparticle-migration, and in vivo investigation.

2. MATERIALS AND CHEMICAL REAGENTS

Chitosan ($C_6H_{11}NO_4$; 161.16 g mol^{-1}; ≥98% purity) and titanium(IV) isopropoxide ($C_{12}H_{28}O_4Ti$; 284.22 g mol^{-1}; 97% purity) were procured from Matrices Enterprises, Nagercoil, Tamil Nadu, India. Fresh banana flower spathes were obtained from a local market.

2.1 Green-assisted Preparation of TiO_2 Nanoparticles Using Banana Flower Spathe Extract

Figure 1 illustrates the preparation of TiO_2 NPs. Banana flower spathe powder (6 g) was heated in 100 mL of deionized water, cooled, filtered, and retained as the plant extract (Suresh *et al.* 2025). Subsequently, 10 mL of TTIP was introduced dropwise into 40 mL of the extract at continuous stirring. The mixture was stirred for 2 h to promote precursor hydrolysis and condensation. Bioactive compounds in the extract assisted particle stabilization rather than reducing titanium ions. Formation of a white suspension indicated the generation of hydrated titanium oxide. The precipitate was separated by centrifugation, repeatedly washed with ethanol and deionized water, and dried at 80 °C (Nazari *et al.* 2025). Finally, the dried powder was calcined at 450 °C for 2 h to obtain crystalline TiO_2 NPs suitable for incorporation into chitosan-based tissue-engineering films.

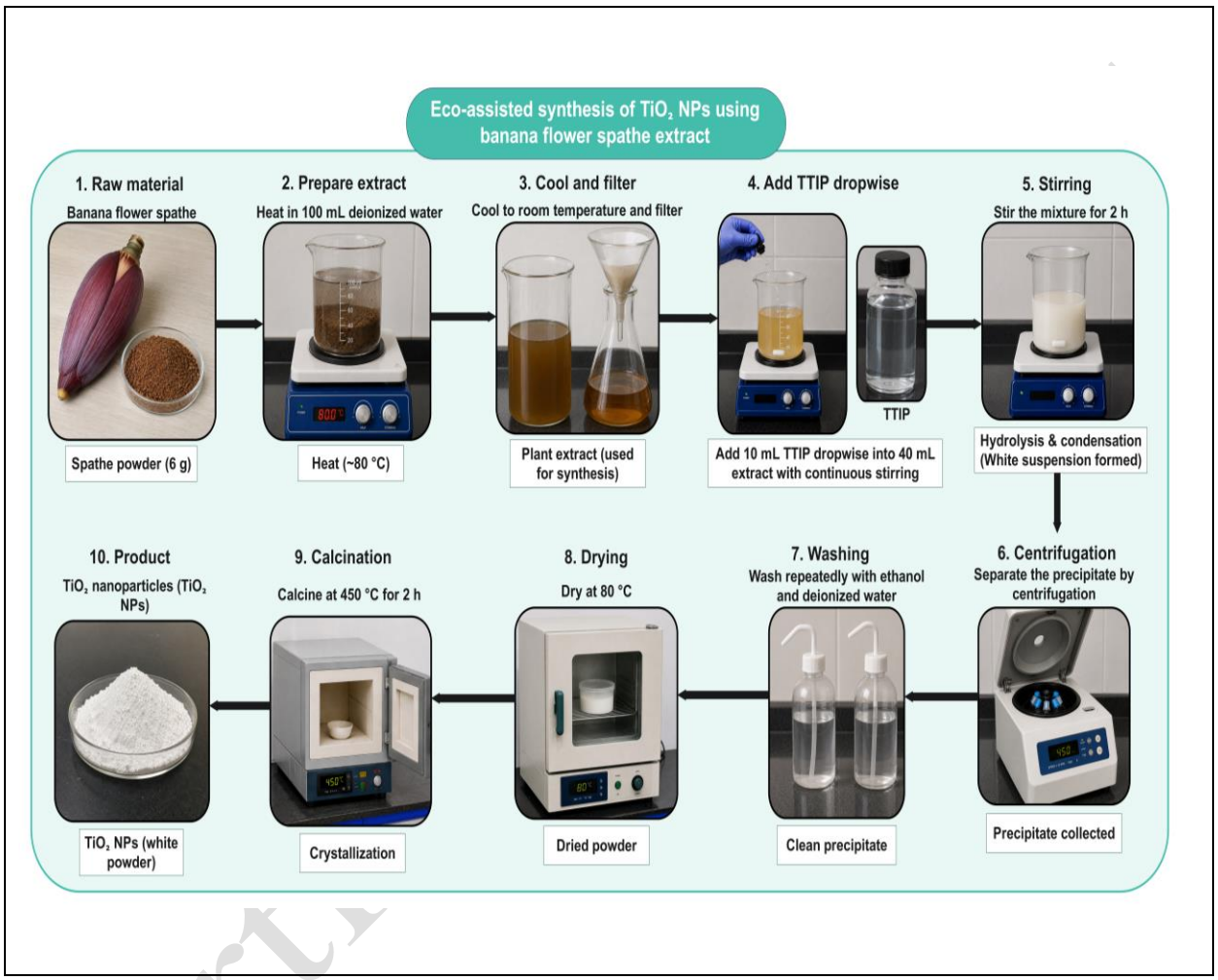

Fig. 1: Eco-assisted synthesis of TiO_2 NPs using banana flower spathe extract

2.2 Chitosan/TiO_2 Nanocomposite-film Fabrication

Figure 2 presents the solution-casting procedure used to fabricate chitosan/TiO_2 nanocomposite films. Chitosan (3 g) was dissolved in 100 mL of 1% (v/v) acetic acid and stirred at 50 °C for 6 h until a uniform solution was obtained (Ma *et al.* 2025). Separately, the TiO_2 NP suspension was ultrasonicated for 30 min to minimize agglomeration. The dried TiO_2 nanoparticles were dispersed in deionized water at a concentration of 10 mg mL^{-1} and ultrasonicated at 40 kHz and 200 W for 30 min. Accordingly, 5, 10, and 20 mL of suspension provided 50, 100, and 200 mg of TiO_2 nanoparticles, respectively. A 5mL portion of the suspension was gradually incorporated into the chitosan solution under continuous stirring. The mixture was stirred at ambient temperature for 12 h and cast into a Petri dish. Drying was performed at 50 °C for 12 h, after which the film was carefully removed. The films were conditioned at 25 ± 2 °C and 50 ± 5% relative humidity for 48 h. Film thickness was measured at five positions using a digital micrometer and averaged before testing. The same protocol was followed using 10 and 20 mL of TiO_2 NP suspension. The final volume of each film-forming solution was adjusted to 120 mL using deionized water. The formulations containing 50, 100, and 200 mg of TiO_2 were designated CT-5, CT-10, and CT-20, respectively, while neat chitosan served as the control. (Subbarao *et al.* 2026).

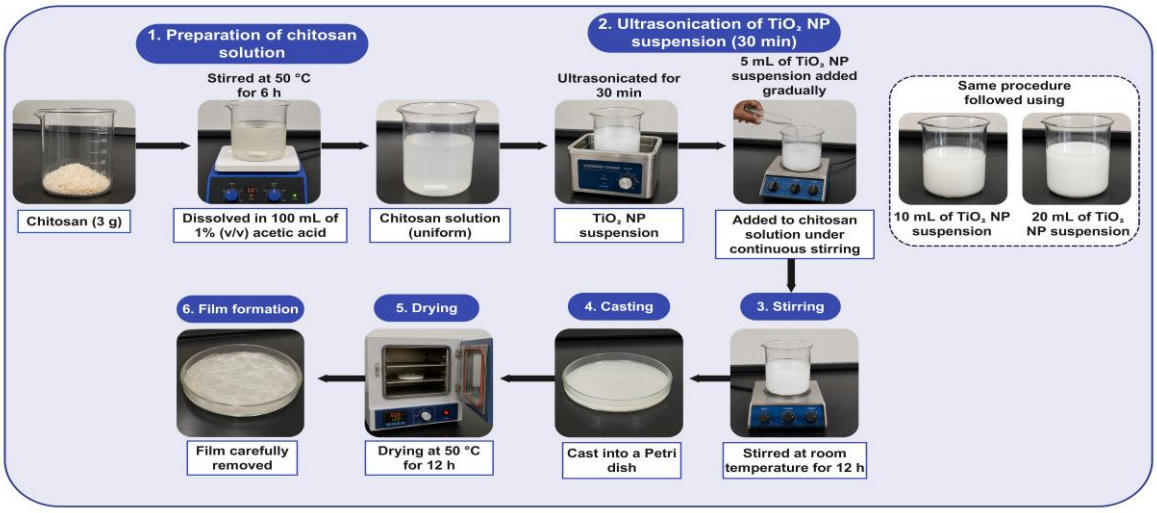

Fig. 2: Schematic illustration of chitosan/TiO_2 nanocomposite-film fabrication by solution casting

2.3 Biological Evaluation

2.3.1 Swelling

Swelling was determined using phosphate-buffered saline (PBS, pH 7.4) to represent physiological conditions. A pre-weighed piece of chitosan/TiO_2 (10 mL) film was immersed in 10 mL of PBS for 24 h at 30 °C. The hydrated specimen was removed, gently blotted to eliminate surface liquid, and immediately weighed. Three specimens were examined to obtain reliable results. The swelling degree was calculated using Eq. (1) (Krishnasamy *et al.* 2026):

$$\text{Swelling degree } (\%) = \frac{W_s - W_d}{W_d} \times 100 \ldots (1)$$

where W_d represents the initial dry mass and W_s denotes the mass after swelling.

2.3.2 *In vitro* Degradation

Film degradation was assessed in PBS over five days. Chitosan/ TiO_2 (10 mL) specimens measuring 2.4 × 2.4 cm were initially dried, weighed (M_0), and immersed separately at 25 mL of PBS. Following incubation, the samples were collected, washed gently, and dried at 50 °C for 1 day before determining residual mass (M_t). Percentage mass loss was obtained using Eq. (2) (Kumar *et al.* 2026):

$$\text{Mass loss } (\%) = \frac{M_0 - M_t}{M_0} \times 100 \quad \ldots (2)$$

2.4 Characterization

The crystalline structure of the films was analysed using a PANalytical X'Pet PRO diffractometer operated over $2\theta = 10 - 80°$ at a scanning rate of $5°\text{min}^{-1}$. Functional groups ere examined using a PerkinElmer Spetrum ToTIR spectrometer between 4000 an 40 cm^{-1} atresolution of 4 cm^{-1} (Kashyap *et al.* 2025). Elemental composition and surface morphology were evaluated by a Gemini Zeiss scanning electron microscope equipped with an EDS detector. EDS analysis was used to verify the presence and distribution of titanium within the film.

Mechanical properties were measured using an Instron 3365 universal testing machine according to ASTM D882. Rectangular specimens measuring 100 × 10 mm were tested at ambient temperature using a crosshead speed of 2 mm min^{-1}. Antibacterial activity against *Staphylococcus aureus* and *Escherichia coli* was determined using the agar-disc diffusion technique by measuring inhibition-zone diameter after incubation.

2.5 DPPH radical-scavenging Activity

Separate film blanks containing film extract and methanol without DPPH were measured at 517 nm to correct nanoparticle scattering and intrinsic sample absorbance. The corrected sample absorbance was calculated as $A_c = A_s - A_b$, where A_s is the film-extract/DPPH absorbance and A_b is the corresponding film-blank absorbance. DPPH inhibition was calculated using(Piryaei *et al.* 2026):

$$\text{DPPH inhibition } (\%) = \frac{A_0 - A_c}{A_0} \times 100 \quad \ldots (3)$$

where A_0 represents the DPPH control absorbance.

2.6 Titanium-release Study

The chitosan/ TiO_2(10 mL) film was dipped at 80 mL of PBS at 37°C for 16 h. At predetermined intervals, aliquots were withdrawn and replaced with equal volumes of fresh PBS. Released titanium was quantified using an Agilent 5110 ICP-OES instrument. UV-visible spectroscopy alone is unsuitable for accurately determining dissolved titanium ions. Cumulative release was calculated using (Mousavi *et al.* 2025):

$$Q_t = C_t V + \sum_{i=1}^{t-1} C_i V_s \quad \ldots (4)$$

where Q_t is the cumulative amount released, C_t were the concentration at time t, V were the total medium volume, and V_s is the sampled volume.

2.7 Functional Role of Banana Flower Spathe Extract

Banana flower spathe extract contains phenolic compounds, flavonoids, tannins, and other plant metabolites that can regulate TTIP hydrolysis and limit excessive TiO_2 particle aggregation during synthesis. These compounds may also contribute to the radical-scavenging response when surface-bound phytochemicals remain after nanoparticle processing (Suchitra *et al.* 2026).

The antibacterial performance of the nanocomposite film involves:

Membrane interaction: Protonated amino groups in chitosan interact with negatively charged bacterial surfaces, increasing membrane permeability.

Reactive oxygen species generation: Under suitable irradiation, TiO_2 NPs can produce reactive oxygen species that damage cellular membranes, proteins, and nucleic acids.

Surface-contact effects: Dispersed TiO_2 NPs increase contact between the film and bacterial cells, potentially restricting cellular metabolism and growth.

2.8 Statistical Analysis

All quantitative experiments were conducted using independent replicates. Tensile testing employed five specimens per formulation, whereas antibacterial and DPPH assays were performed in triplicate. Results were expressed as mean ± standard deviation. Statistical differences were evaluated using one-way ANOVA followed by Tukey's multiple-comparison test, with $p < 0.05$ considered statistically significant.

3. RESULTS AND DISCUSSION

3.1 UV–visible Analysis of TiO_2 Nanoparticles

UV–visible spectroscopy was employed to examine the optical characteristics of the biosynthesized TiO_2 NPs over the wavelength range of 250–800 nm. During TTIP hydrolysis, the initially transparent reaction mixture gradually developed into a milky-white suspension, indicating the formation of hydrated titanium oxide. Unlike metallic nanoparticles, TiO_2 NPs do not exhibit a surface-plasmon-resonance band in the visible region. As shown in Fig. 3, the prepared TiO_2 NPs displayed a distinct absorption edge at approximately 330 nm, which was assigned to electron excitation from the valence band to the conduction band. Similarly, TiO_2–Fe_2O_3–chitosan nanocomposites synthesized using Moringa oleifera extraction showed an absorption peak at 243 nm in UV- Vis analysis (Rajamehala *et al.* 2023). Banana flower spathe extract exhibited absorption mainly within the ultraviolet region because of its phytochemical constituents. The progressive increase in UV absorption during processing indicated the formation and increasing concentration of titanium oxide particles. The optical band-gap energy may be estimated from the absorption data using the Tauc relation and is expected to be approximately 3.76 eV for anatase-dominant TiO_2.

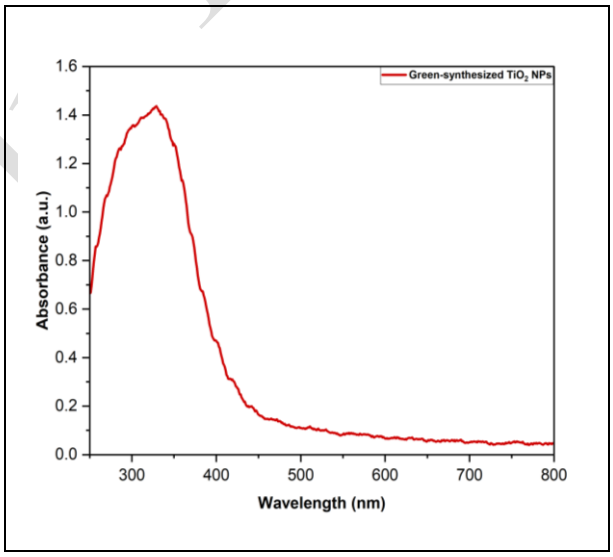

Fig. 3: UV–visible absorption spectrum of banana flower spathe-mediated TiO_2 nanoparticles

3.2 XRD Phase and Structural Analysis

Figure 4 presents the XRD profile of the neat chitosan film. Broad diffraction features near 2θ= 10.44° and 20.10° indicate its partially crystalline polymer structure, arising from ordered regions maintained by intermolecular hydrogen bonding. The TiO_2 NP pattern exhibited reflections at approximately 25.30°, 37.82°, 48.02°, 53.93°, 55.10°, 62.72°, 68.72°, 70.33°, and 75.16° indexed to the (101), (004), (200), (105), (211), (204), (116), (220), and (215) planes, respectively. These reflections were indexed to the tetragonal anatase TiO_2 phase according to JCPDS/ICDD Card No. 21-1272.

Figures 4 display the diffraction patterns of chitosan films containing 5, 10, and 20 mL of TiO_2 NP suspension, respectively. At 5 mL, the TiO_2 reflections were weak because of the low nanoparticle concentration and dominant amorphous polymer background. The characteristic peaks became distinguishable at 10 mL and more intense at 20 mL, confirming the concentration-dependent incorporation of crystalline TiO_2 into the chitosan matrix.

The broad chitosan reflection remained visible in every nanocomposite, although its position and intensity changed slightly because TiO_2 disrupted the original polymer-chain arrangement. Scherrer analysis of the TiO_2 (101) reflection produced an average crystallite size of 18.6 ± 1.3 nm. The calculated crystallinity indices of neat chitosan, CT-5, CT-10, and CT-20 were 27.4%, 29.2%, 31.7%, and 34.6%, respectively. The concentration-dependent increase confirmed the contribution of crystalline anatase TiO_2 to the polymer matrix. Likewise, magnesium oxide nanoparticles synthesized using Clerodendrum inerme bast fiber extract exhibited crystallite sizes of 22–34 nm(Ganvir *et al.* 2026). These structural changes may influence mechanical performance, but this relationship must be confirmed using tensile-test results.

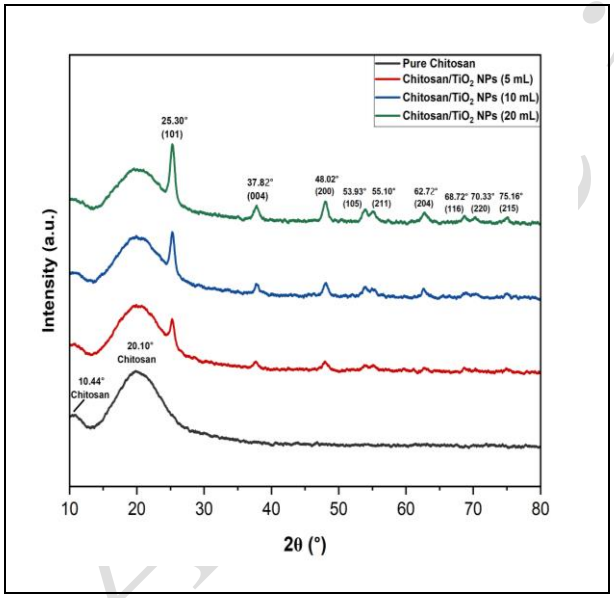

Fig. 4: XRD profiles of neat chitosan, chitosan/TiO_2 nanocomposite films containing 5, 10, and 20 mL of TiO_2 NP suspension

3.3 FTIR Functional-group Analysis

Figure 5 compares the FTIR spectra of neat chitosan and the prepared chitosan/TiO_2 films. Neat chitosan showed a broad absorption band at approximately 3352 cm^{-1}, overlapping O–H and N–H stretching vibrations associated with hydrogen bonding. The band at 2912 and 2875 cm^{-1} corresponded to asymmetric and symmetric aliphatic C–H stretching, respectively. Signals observed near 1624 and 1587 cm^{-1} were assigned to amide-I vibration and N–H bending of the amino groups. The bands at approximately 1422 and 1377 cm^{-1} represented CH_2 and CH_3 deformation. Saccharide-structure vibrations appeared at 1152 cm^{-1} for C–O–C stretching and at 1072 and 1036 cm^{-1} for C–O stretching.

The spectra of films containing 5, 10, and 20 mL of TiO_2 NP suspension. Incorporation of TiO_2 produced slight shifts and intensity changes in the O–H/N–H, amide-I, and amino-group bands, indicating interfacial bonding or coordination between nanoparticles and chitosan chains. Increasingly pronounced absorption region between approximately 520 and 675 cm^{-1} was assigned to Ti–O and Ti–O–Ti lattice vibrations. Its intensity increased with TiO_2 content, supporting nanoparticle incorporation. The results indicate physicochemical interactions without the formation of new covalent bonds. The O–H/N–H band shifted from 3352 cm^{-1} in neat chitosan to 3346, 3338, and 3329 cm^{-1} in CT-5, CT-10, and CT-20, respectively. The amide-I band similarly shifted from 1624 to 1620, 1617, and 1614 cm^{-1}. These systematic shifts indicate progressively stronger hydrogen-bonding and coordination interactions between chitosan and TiO_2.

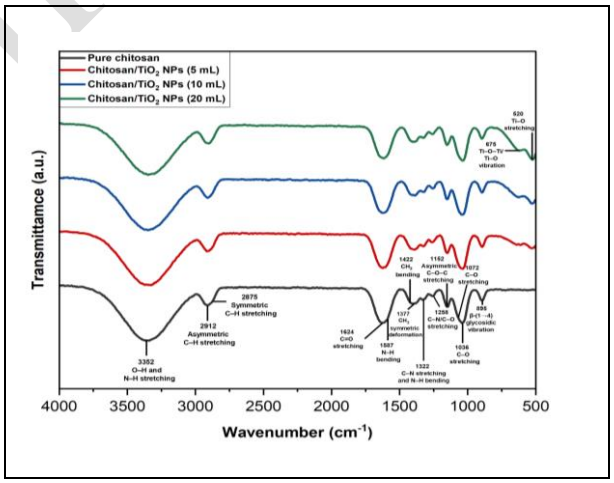

Fig. 5: FTIR spectra of (a) chitosan and chitosan/TiO_2 films (b) 5, (c) 10 and (d) 20 mL of TiO_2 NP suspension

3.4 SEM Morphological Analysis

Figure 6 presents the SEM image of neat chitosan and chitosan/TiO_2 nanocomposite films. The neat chitosan specimen in Fig. 6(a) exhibited a comparatively compact, sheet-like morphology with relatively smooth regions. Minor pores, surface irregularities, and localized granular residues were also observed, possibly resulting from solvent evaporation, film fracture, or sample preparation. Incorporation of TiO_2 altered the chitosan morphology and increased the apparent surface heterogeneity.

The film containing 5 mL of TiO_2 NP suspension exhibited fine surface deposits together with localized particle clusters and small cavities. At 10 mL, a comparatively compact matrix containing relatively well-distributed fine particles was observed, although some pores and larger particles remained near the specimen edges. Increasing the TiO_2 suspension volume to 20 mL produced extensive agglomeration, irregular clusters, voids, and reduced matrix continuity, which may have resulted from stronger particle–particle interactions at higher loading. The comparatively compact morphology of the 10 mL formulation is consistent with its improved tensile strength and antibacterial activity. In contrast, the pronounced agglomeration observed at 20 mL may have created stress-concentration regions, contributing to the lower tensile strength relative to the 10 mL film. The antibacterial activity of the TiO_2-containing films may involve surface interactions and, under suitable irradiation, the generation of reactive oxygen species.

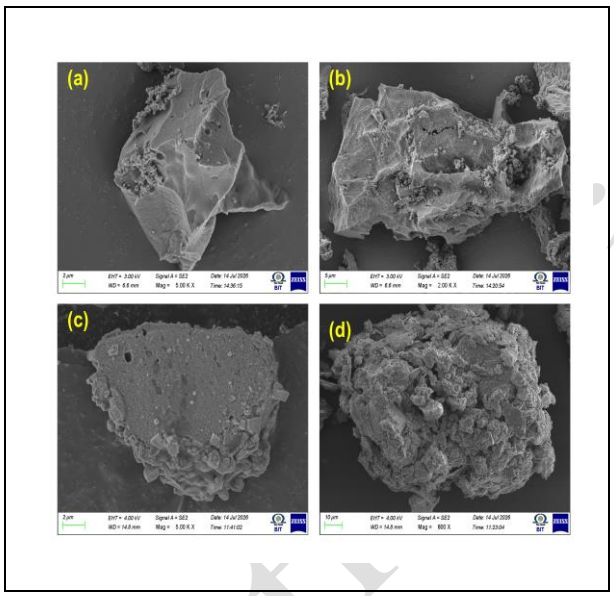

Fig. 6: SEM micrographs of (a) chitosan and chitosan/TiO_2 nanocomposite films (b) 5, (c) 10, and (d) 20 mL of TiO_2 NP suspension

3.5 EDX Elemental Analysis

Figure 7 presents the EDX of neat chitosan and the chitosan/TiO_2 films. Spectrum of neat chitosan in Fig. 7(a) predominantly contained carbon, oxygen, and nitrogen, consistent with the elemental composition of the polymer. Their approximate weight percentages were 61.41%, 28.13%, and 10.46%, respectively.

A characteristic Ti Kα signal at approximately 4.51 keV confirmed TiO_2 incorporation. Titanium contents increased from 11.00 wt.% in CT-5 to 18.03 wt.% in CT-10 and 25.94 wt.% in CT-20. The corresponding carbon, oxygen, nitrogen, and titanium contents were 54.65, 25.04, 9.31, and 11.00 wt.% for CT-5; 50.34, 23.07, 8.56, and 18.03 wt.% for CT-10; and 45.48, 20.84, 7.74, and 25.94 wt.% for CT-20. The progressive titanium increase agreed with the nominal suspension loading. The titanium contents were approximately 11.00, 18.03, and 25.94 wt.% for films prepared with 5, 10, and 20 mL of TiO_2 suspension, respectively. The progressive increase in titanium content agreed with the increasing nanoparticle loading. Carbon and oxygen remained the principal elements in all films, while nitrogen originated from the amino groups of chitosan.

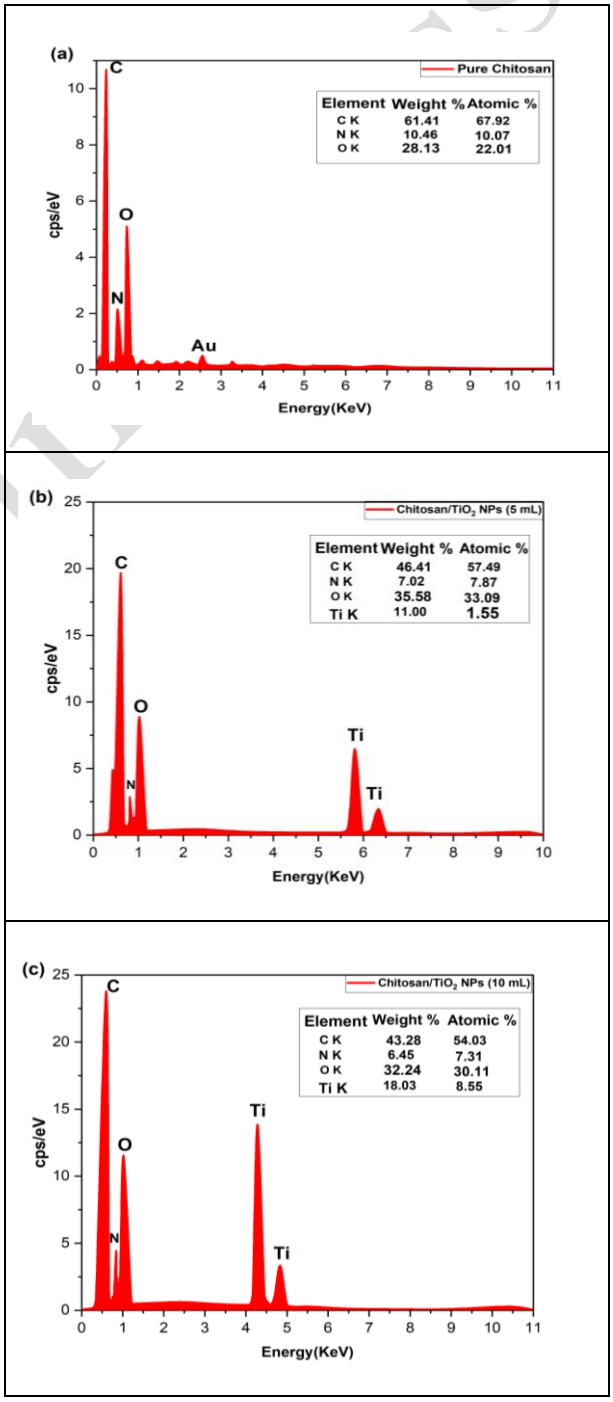

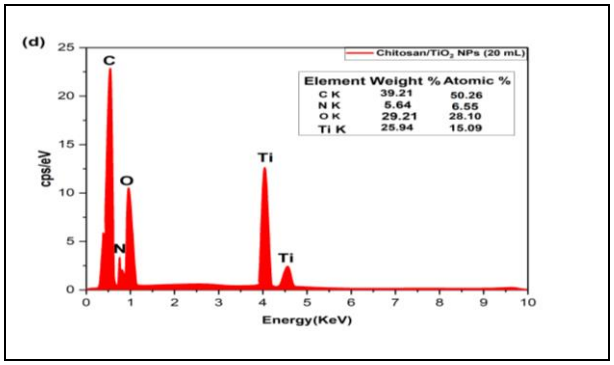

Fig. 7: EDX spectra of (a) chitosan and chitosan/TiO_2 films (b) 5, (c) 10 and (d) 20 mL of TiO_2 NP suspension

3.6 Swelling Behavior

Figure 8 illustrates the time-dependent swelling response of the chitosan/TiO_2 (10mL) nanocomposite film in PBS at pH 7.4. Rapid fluid absorption occurred during the initial stage, with swelling increasing from approximately 475% after 1 h to 505% after 4 h. After approximately 3 h, only a minor change was observed, indicating that the film had approached swelling equilibrium.

Water uptake primarily resulted from interactions between the aqueous medium and the hydrophilic amino and hydroxyl groups of chitosan. Incorporation of TiO_2 NPs altered the spacing and free volume between polymer chains, allowing PBS to penetrate the film network. Simultaneously, hydrogen bonding between TiO_2 and chitosan restricted excessive chain relaxation and helped the film retain its structural integrity during hydration.

The controlled swelling of the 10 mL formulation could support moisture retention and molecular transport without causing rapid film disintegration. These properties are favourable for potential wound-contact and tissue-support applications. However, cell infiltration, attachment, and proliferation must be verified separately through appropriate biological experiments.

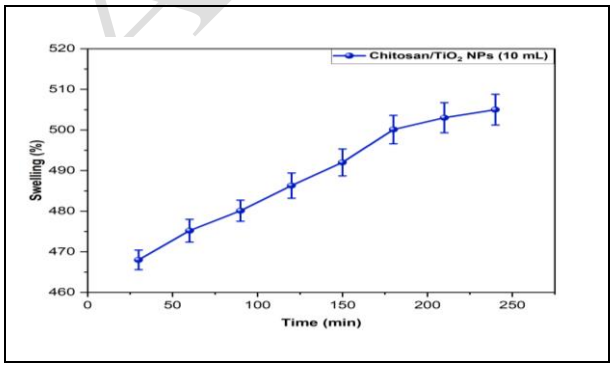

Fig. 8: Swelling profile of chitosan/TiO_2 nanocomposite film in PBS at pH 7.4

3.7 *In vitro* Degradation Behaviour

Controlled degradation is important for temporary tissue-support materials because structural stability should be retained during the initial healing stage and gradually reduced thereafter. Figure 9 presents the mass-loss profile of the chitosan/TiO_2 (10 mL) film during five days of incubation in PBS. The film exhibited approximately 5.8% mass loss after the first day, which progressively increased to nearly 18.6% by day 5.

The observed mass reduction was associated with water penetration, relaxation of chitosan chains, and dissolution of weakly bound polymer fractions. TiO_2 NPs interacted with the amino and hydroxyl groups of chitosan, restricting rapid chain separation and enabling more gradual degradation. Nevertheless, prolonged hydration weakened the polymer network and progressively reduced film integrity.

A very rapid degradation rate may cause premature structural failure, whereas excessively slow degradation can interfere with tissue remodelling and material integration. The moderate mass-loss behaviour of the 10 mL formulation indicates potential for temporary tissue-support applications. However, long-term enzyme-assisted degradation and cytocompatibility investigations are required before biomedical suitability can be confirmed.

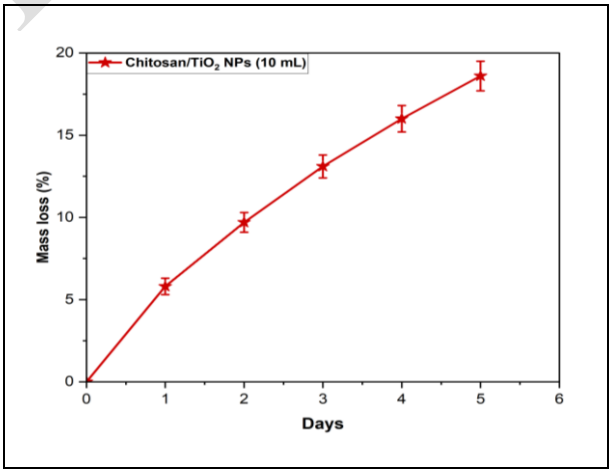

Fig. 9: *In vitro* mass loss of the chitosan/TiO_2 (10 mL) nanocomposite film during five-day incubation in PBS

3.8 Tensile Properties

Mechanical stability is essential for films intended to provide temporary support during tissue repair. Figure 10 (a & b) compares elongation at break and tensile strength of neat chitosan and chitosan/TiO_2 nanocomposite films. Neat chitosan exhibited a tensile strength of 31.80 ± 1.40 MPa, while the 5 and 10 mL formulations showed 39.70 ± 1.60 and 48.90 ± 1.80 MPa, respectively. In previous study, Chitosan composite films

containing 4.76% honeysuckle extract/attapulgite nanocomposites achieved a tensile strength of 24.9 ± 2.35 MPa, elongation at break of 64.8 ± 2.11% (Gao *et al.* 2024). The improvement obtained for the 10 mL formulation was associated with comparatively uniform nanoparticle dispersion and effective interfacial interaction between TiO_2 and the polymer chains. These interactions restricted chain movement and facilitated stress transfer throughout the film.

Increasing the TiO_2 suspension to 20 mL reduced the tensile strength to 42.30 ± 1.70 MPa. At higher loading, particle agglomeration produced stress-concentration regions that promoted earlier failure. Elongation at break decreased from 29.60 ± 1.20% for neat chitosan to 26.80 ± 1.10%, 23.50 ± 0.90%, and 18.90 ± 0.80% for the 5, 10, and 20 mL formulations, respectively. This reduction indicated that TiO_2 reinforcement increased film rigidity while limiting polymer-chain mobility. Consequently, the 10 mL film provided the best balance between strength and flexibility.

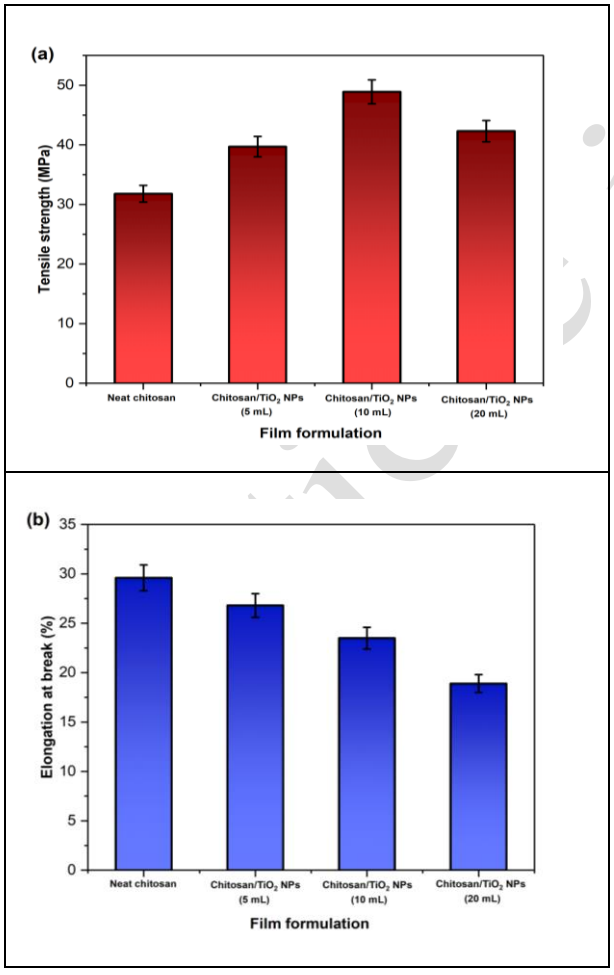

Fig. 10: Mechanical properties of neat chitosan and chitosan/TiO_2 films containing 5, 10, and 20 mL of TiO_2 NP suspension: (a) tensile strength and (b) elongation at break

At the highest TiO_2 loading, nanoparticle agglomeration weakened interfacial contact with the chitosan matrix and generated localized stress-concentration regions. Figure 11 compares the stress–strain responses of neat chitosan and the three chitosan/TiO_2 nanocomposite films.

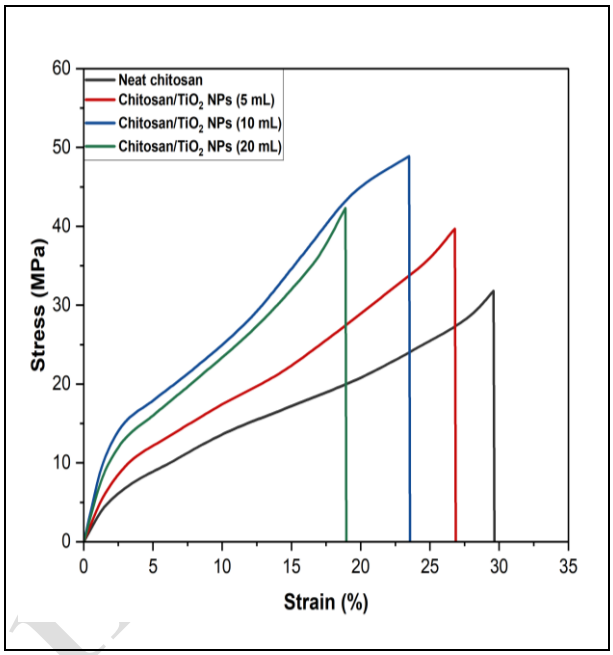

Fig. 11: Stress–strain profiles of neat chitosan and chitosan/TiO_2 nanocomposite films containing 5, 10, and 20 mL of TiO_2 NP suspension

3.9 Electrical Impedance Analysis

Electrochemical impedance spectroscopy was employed to determine the electrical resistance and conductivity of neat chitosan and the chitosan/TiO_2 nanocomposite films. Figure 12 presents their Nyquist plots, consisting of a depressed semicircle in the high-frequency region followed by an inclined tail at lower frequencies. The semicircular response represents bulk charge-transfer resistance, whereas the low-frequency region is associated with electrode polarization and interfacial effects.

Bulk resistance (R_b) was obtained from the real-axis intercept of the fitted semicircle. Electrical conductivity was subsequently calculated using Eq. (5) (Tiwari *et al.* 2026):

$$\sigma = \frac{t}{AR_b} \quad \ldots (5)$$

where σ is the electrical conductivity in Scm^{-1}, t denotes film thickness in cm, A represents the electrode-film contact area in cm^2, and R_b is the bulk resistance in Ω. The corresponding resistance and conductivity results are provided in Table 1.

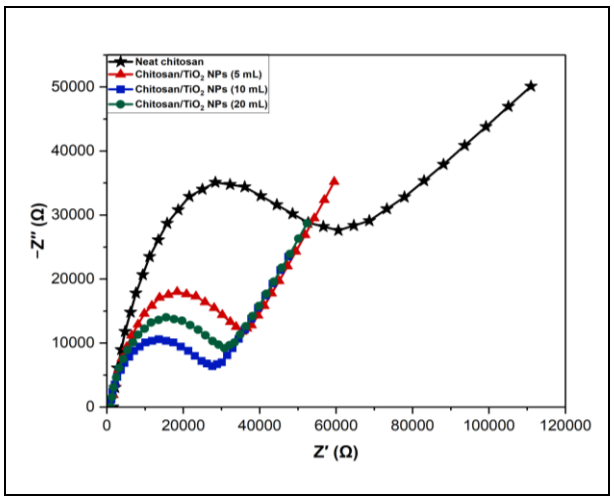

Fig. 12: Nyquist plots of neat chitosan and chitosan/TiO_2 nanocomposite films containing 5, 10, and 20 mL of TiO_2 NP suspension

Table 1 compares the electrical conductivity of neat chitosan and the prepared chitosan/TiO_2 films. Neat chitosan exhibited a relatively low conductivity of 1.90×10^{-8} S cm^{-1}. Incorporating 5 and 10 mL of TiO_2 NP suspension increased the conductivity to 2.60×10^{-7} and 6.80×10^{-7} S cm^{-1}, respectively. This enhancement was attributed to the semiconducting behaviour of TiO_2 and improved interfacial charge transport within the polymer matrix.

At 20 mL, conductivity declined to 4.90×10^{-7} S cm^{-1}. Excessive nanoparticle loading promoted agglomeration, disrupted uniform transport pathways, and increased interfacial resistance. Consequently, the 10 mL formulation exhibited the lowest bulk resistance and highest conductivity.

Although the optimized film showed improved electrical behaviour, its conductivity remained within the semiconducting or weakly conductive range. Therefore, its ability to promote electrical signalling, cellular alignment, proliferation, or differentiation must be established through electrical-stimulation and cell-culture investigations rather than inferred solely from conductivity measurements.

Table 1. Electrical properties of neat chitosan and chitosan /TiO_2 nanocomposite films

Film Formulation	Electrical Conductivity (Scm^{-1})
Neat chitosan	1.90×10^{-8}
Chitosan /TiO_2(5 mL)	2.60×10^{-7}
Chitosan/ TiO_2(10 mL)	6.80×10^{-7}
Chitosan /TiO_2(20 mL)	4.90×10^{-7}

3.10 Antibacterial Activity

Figure 13 and Table 2 present the antibacterial performance of neat chitosan and chitosan/TiO_2 nanocomposite films against *Staphylococcus aureus* and *Escherichia coli*. Neat chitosan produced limited inhibition, associated with interactions between its protonated amino groups and negatively charged bacterial surfaces. Incorporating TiO_2 NPs substantially increased the inhibition zones.

The 10 mL formulation produced the strongest response with inhibition zones of 18.2 mm against *S. aureus* and 19.0 mm against *E. coli*. In a prior study, methylcellulose/chitosan nanofiber films incorporating Ag-MOF-LAC nanoparticles achieved inhibition zones of 19.8 ± 5.2 mm against *E. coli* and 20.1 ± 3.2 mm against *S. aureus* (Tavassoli *et al.* 2024). Its performance was associated with comparatively uniform nanoparticle dispersion and effective contact with bacterial cells. TiO_2 can generate reactive oxygen species under suitable irradiation, causing membrane oxidation, protein inactivation, respiratory disruption, and nucleic acid damage. Chitosan may complement this action by increasing membrane permeability.

Increasing the TiO_2 suspension to 20 mL did not provide further improvement. Particle agglomeration probably reduced the exposed active surface and limited contact between TiO_2 and microorganisms. Differences between the bacterial strains were associated with their distinct cell-envelope structures; however, sensitivity cannot be predicted solely from Gram classification. Overall, the 10 mL film demonstrated the best antibacterial response among the tested formulations and may be considered for further wound-contact and tissue-support evaluation.

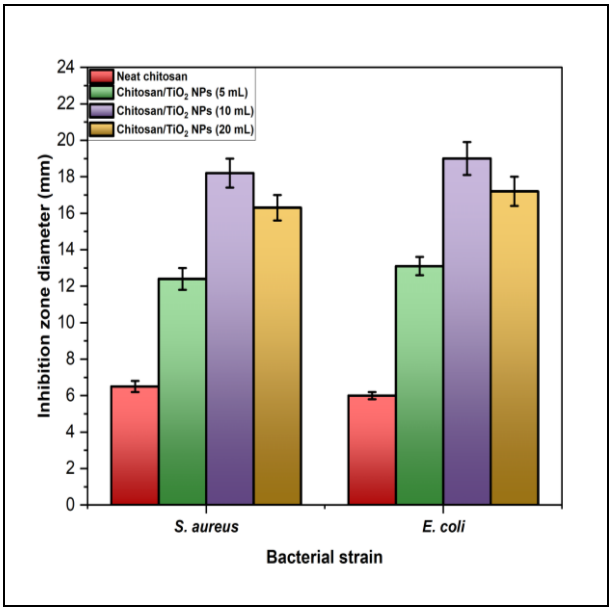

Fig. 13: Antibacterial activity of (a) chitosan and chitosan/TiO_2 nanocomposite films (b) 5, (c) 10 and (d) 20 mL of TiO_2 NP suspension

Table 2. Inhibition-zone diameters of neat chitosan and chitosan/TiO_2 nanocomposite films

Bacterial strain	Neat chitosan (mm)	Chitosan/TiO_2 (5 mL) (mm)	Chitosan/TiO_2 (10 mL) (mm)	Chitosan/TiO_2 (20 mL) (mm)
S. aureus	6.5	12.4	18.2	16.3
E. coli	6.0	13.1	19.0	17.2

The 10 mL formulation produced significantly larger inhibition zones against both bacterial strains than the remaining formulations ($p < 0.05$).

3.11 Antioxidant Activity

Table 3 compares the DPPH radical-scavenging activities of TiO_2 NPs, neat chitosan, and the chitosan/TiO_2 (10 mL) nanocomposite film. TiO_2 NPs exhibited limited scavenging activity of approximately 18%, whereas neat chitosan produced 34% inhibition. The nanocomposite film showed the highest activity of 48%, indicating that nanoparticle incorporation modified the radical-interaction behaviour of the polymer matrix.

The response of chitosan may originate from its amino and hydroxyl groups, which can participate in hydrogen or electron transfer. However, TiO_2 is primarily photocatalytic and can generate reactive oxygen species under irradiation; therefore, it should not automatically be described as an antioxidant. Nanoparticle scattering can also affect absorbance measurements at 517 nm. Film and nanoparticle blanks should consequently be subtracted before calculating DPPH inhibition. The antioxidant performance must be confirmed experimentally before suggesting biomedical applicability.

Table 3. DPPH radical-scavenging activity of TiO_2 NPs, neat chitosan, and the chitosan/TiO_2 film

Sample	Absorbance at 517 nm	DPPH Inhibition (%)
Control	0.122	—
TiO_2 nanoparticles	0.105	13.93 ± 1.12%
Neat chitosan	0.084	31.15 ± 1.46%
CT-10	0.067	45.08 ± 1.73%

3.12 *In vitro* Titanium-release Behaviour

The release behaviour of the chitosan/TiO_2 (10 mL) nanocomposite film was evaluated in phosphate-buffered saline at 37 °C. Figure 14 shows gradual raise in cumulative titanium release with incubation. Approximately 2.2% was released during the initial 4 h, followed by a slower release phase that reached nearly 4.7% after 12 h. The absence of a pronounced burst indicated that most TiO_2 NPs remained immobilized within the chitosan network. Initial release originated from weakly bound particles near the film surface, whereas subsequent release was controlled by PBS penetration, polymer-chain relaxation, and progressive matrix degradation. This sustained profile may help maintain film functionality while limiting rapid nanoparticle loss. However, cytocompatibility and particle-migration studies are required before biomedical safety can be established. ICP-OES quantified total released titanium but did not differentiate dissolved titanium species from intact or agglomerated TiO_2 nanoparticles. Therefore, the observed 4.7% release cannot independently establish nanoparticle immobilization or biological safety. Cytotoxicity, oxidative stress, cellular uptake, transwell migration, hemocompatibility, and long-term release studies are required before tissue-contact safety can be confirmed.

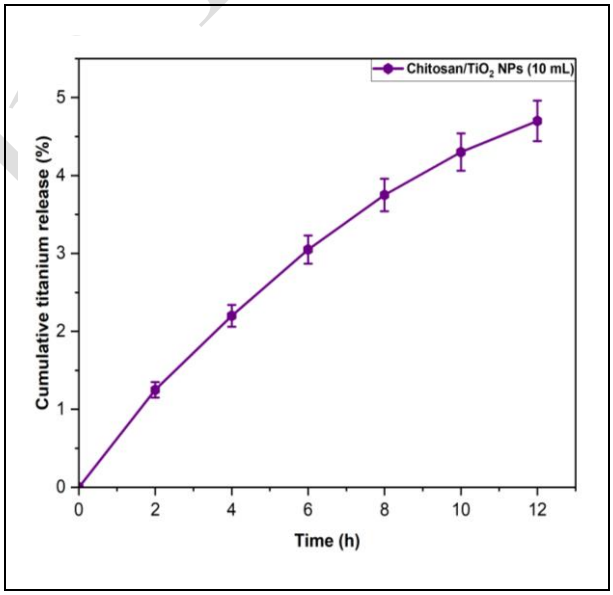

Fig. 14:Cumulative titanium release from the chitosan/TiO_2 (10 mL) nanocomposite film in PBS at 37 °C

4. CONCLUSION

Banana flower spathe-assisted TiO_2 nanoparticles were successfully incorporated into chitosan films. UV–visible analysis showed an absorption edge near 330 nm, while XRD, FTIR, SEM, and EDX supported TiO_2 incorporation into the chitosan matrix. The 10 mL formulation exhibited the best overall performance, including a tensile strength of 48.9 MPa, conductivity of 6.80×10^{-7} S cm^{-1}, approximately 505% equilibrium swelling, 18.6% mass loss after five days, and 4.7% titanium release after 12 h. It produced

inhibition zones of 18.2 and 19.0 mm against *S. aureus* and *E. coli*, respectively. These findings demonstrate the film's promising mechanical, physicochemical, and antibacterial properties. However, its suitability for tissue-regeneration or wound-contact applications cannot be confirmed without cytotoxicity, cell-adhesion, hemocompatibility, nanoparticle-migration, long-term degradation, and in vivo investigations.

FUNDING

This research received no specific grant from any funding agency in the public, commercial, or not-for-profit sectors.

CONFLICTS OF INTEREST

The authors declare that there is no conflict of interest.

COPYRIGHT

REFERENCES

Alfaifi, M. Y., Reda, E. M., El-Maghraby, R. M., Shati, A. A., Elbehairi, S. E. I. and Elshaarawy, R. F. M., Green-engineered multifunctional antimicrobial and UV-shielding fabrics using mono- and bimetallic ionic chitosan composite nanogels, *J. Umm Al-Qura Univers. Appl. Sci.*, (2025). https://doi.org/10.1007/s43994-025-00265-y

Ali, M. H., Dutta, S. K., Sultana, M. S., Habib, A. and Dhar, P. K., Green synthesized CeO_2 nanoparticles-based chitosan/PVA composite films: Enhanced antimicrobial activities and mechanical properties for edible berry tomato preservation, *Int. J. Bio. Macromol.*, 280, 135976(2024). https://doi.org/10.1016/j.ijbiomac.2024.135976

Alzahrani, A., Fluorescent carbon dots in situ polymerized biodegradable semi-interpenetrating tough hydrogel films with antioxidant and antibacterial activity for applications in food industry, *Food Chem.,* 447, 138905(2024). https://doi.org/10.1016/j.foodchem.2024.138905

Alzahrani, S. O., Alisaac, A., Alsahag, M., Aldosari, F. M., Alshammari, N. M., Alhalafi, M. H., Obaid, A. O. and El-Metwaly, N. M., Green synthesis, characterization, phytochemical analyses, and antibacterial evaluation of Ag/TiO_2 and Ag/TiO_2-chitosan nanocomposites derived from M. chamomilla, *Int, J. Bio. Macromol.*, 312, 144220(2025). https://doi.org/10.1016/j.ijbiomac.2025.144220

Balapure, S., Yadav, S. and Rana, P., Green-Synthesized Silver Nanoparticles Integrated Into Chitosan Gelatin Films for Antimicrobial and Biodegradable Food Packaging, *J. Food Process Eng.*, 49(5), e70598(2026). https://doi.org/10.1111/jfpe.70598

Costa, D., Cascione, M., De Matteis, V., Di Corato, R., Gallo, N., Villani, S., Demitri, C., Alifano, P., Sannino, A., Cuniberti, G. and Rinaldi, R., Structural and Physical Properties of Chitosan Films Containing UV-Driven in Situ Growth of Silver Nanoparticles, *ACS Omega*, 11(13), 20213–20226 (2026). https://doi.org/10.1021/acsomega.5c09873

Emam, M., Seif, M. and Hasanin, M. S., Green Synthesis of Curcuminoids-Enriched Trimetallic Nanoparticles Stabilised by Chitosan/Collagen Nanocomposites against Foodborne Pathogens, *Appl. Biochem. Biotechnolog.*, 198(5), 3657–3678 (2026). https://doi.org/10.1007/s12010-025-05565-x

Ganvir, H. V, Musrif, P. G., Satishkumar, P., Kadam, A. D., Saminathan, R. and Krishnaraj, C., Sustainable Synthesis of MgO Nanoparticles from Clerodendrum inerme Bast Fiber Extract: Physicochemical Characterization and Antibacterial Performance, *J. Environ. Nanotechnol.*, 15(2), 380–388(2026). https://doi.org/10.13074/jent.2026.06.2622227

Gao, W., Mu, B., Yang, F., Li, Y., Wang, X. and Wang, A., Multifunctional honeysuckle extract/attapulgite/chitosan composite films containing natural carbon dots for intelligent food packaging, *Int. J. Bio. Macromol.*, 280, 136042(2024). https://doi.org/10.1016/j.ijbiomac.2024.136042

Kashyap, D. N., Jachak, S. R., Khedkar, S. S., Ponnuswamy, M., Suresh, G., Revathi, R. and Mayakannan, S., Impact of Fiber Orientation on the Mechanical Characteristics of Hybrid Banana Palm Amino Composites and AI-based Performance Prediction, *J. Environ. Nanotechnol.*, 14(3), 223–233 (2025). https://doi.org/10.13074/jent.2025.09.2531645

Krishnasamy, B., Gladston, A. K., Sekar, C. B. and Selvaraju, M., Investigation on the thermal, mechanical, and morphological characterization of peepal fiber-reinforced epoxy composites enhanced with micro-particulate ziziphus mauritiana seed powder, *Revista Materia*, 31, e202500643(2026). https://doi.org/10.1590/1517-7076-RMAT-2025-0643

Kumar, V., Kumar, R., Upreti, M., Puri, K. and Satishkumar, P., Development of a Green-synthesized GNP/CQD-reinforced TSP–GG Hydrogel Bead System for pH-sensitive and Sustained Doxorubicin Release in Colorectal Cancer Therapy, *J. Environ. Nanotechnol.*, 15(2), 31–42 (2026). https://doi.org/10.13074/jent.2026.06.2612081

Ma, J., Huang, X., Jin, L. and Xu, Q., Effect of dialdehyde nanocellulose-tannin fillers on antioxidant, antibacterial, mechanical and barrier properties of chitosan films for cherry tomato preservation, *Food Chem.*, 463, 141274(2025). https://doi.org/10.1016/j.foodchem.2024.141274

Meerasri, J., Sukatta, U., Rugthaworn, P., Klinsukhon, K., Khacharat, L., Sakayaroj, S., Chollakup, R. and Sothornvit, R., Synergistic effects of thyme and oregano essential oil combinations for enhanced functional properties of sericin/pectin film, *Int. J. Bio. Macromol.*, 263, 130288(2024). https://doi.org/10.1016/j.ijbiomac.2024.130288

Mousavi, S. F., Arsalani, N. and Ghorbani, M., Preparation of sodium alginate and xanthan gum bionanocomposite films reinforced with hybrid halloysite nanotubes containing ZnO and licorice root extract for wound dressing applications, *Int. J. Bio. Macromol.*, 307, 141974(2025). https://doi.org/10.1016/j.ijbiomac.2025.141974

Nazari, M. S., Labbaf, S., Karbasi, M. and Mohammadzadeh, M., Enhanced skin cancer therapy using green synthesized titanium dioxide-polycaprolactone-chitosan nanostructure loaded with curcumin, *Int. J. Bio. Macromol.*, 334, 149095(2025). https://doi.org/10.1016/j.ijbiomac.2025.149095

Pekdemir, S. S., Taş, N. A., Qader, I. N., Pekdemir, M. E., Babkir, K. A., Taş, R. and Kirbağ, S., Biopolymer-Based Nanocomposite Films: Chitosan/Polycaprolactone Matrix Reinforced with Green-Synthesized Silver NPs, *J. Clust. Sci.*, 36(5), 164(2025). https://doi.org/10.1007/s10876-025-02884-1

Piryaei, M., Shabani, S. and Alipour, K., pH-responsive intelligent edible films based on sodium alginate–pectin reinforced with chitosan nanoparticles, green-synthesized TiO_2 nanoparticles, and Azarshahr red onion peel anthocyanins, *Appl. Food Res.*, 6(2), 102268 (2026). https://doi.org/10.1016/j.afres.2026.102268

Qin, J., Huang, X., Xu, Q. and Jin, L., Active polyvinyl alcohol films with enhanced strength, antioxidant and antibacterial properties by incorporating nanocellulose and tannin, *Int. J. Bio. Macromol.*, 283, 137873 (2024). https://doi.org/10.1016/j.ijbiomac.2024.137873

Rajamehala, M., Kumara Pandian, A. M., Rajasimman, M. and Gopalakrishnan, B., Porous nanocomposites for sorptive elimination of ibuprofen from synthetic wastewater and its molecular docking studies, *Environ. Res.*, 218, 114984(2023). https://doi.org/10.1016/j.envres.2022.114984

Reddy, S. and Venkatachalapathi, N., Investigation of Mechanical Performance and Environmental Degradation of PLA-based Hybrid Composites Containing Natural and Carbonized Fillers, *J. Environ. Nanotechnol.*, 14(4), 454–462 (2025). https://doi.org/10.13074/jent.2025.12.2541798

Shankar, V. and Venkatesh, S., Fabrication and Characterization of Corn Starch-blended Polyhydroxybutyrate Films, *J. Environ. Nanotechnol.*, 14(3), 169–178 (2025). https://doi.org/10.13074/jent.2025.09.2531594

Sokary, R., Raslan, H. A. and Fathy, R. M., Green synthesis of CdS/flaxseed mucilage nanocomposite films using gamma irradiation for packaging applications, *Radiochimica Acta*, 112(6), 427–444 (2024). https://doi.org/10.1515/ract-2023-0251

Subbarao, E., Sharma, D., Singh, P., Gupta, R. K., Gayathri, B. and Mayakannan, S., Influence of B_4C and TiO_2 fillers on mechanical and tribological performance of Canna indica/Curaua fiber reinforced hybrid composites with ANN prediction, *Interact.*, 247(1), 148(2026). https://doi.org/10.1007/s10751-026-02511-z

Subbarayalu, A., Anantharaman, R., Singh, N., Murugesan, R., Sangeetha, N. and Arasavalli, N., Green Synthesized ZnO Incorporated Sida cordifolia/Alginate Hydrogel Scaffolds for Antibacterial Wound Healing Applications, *J. Environ. Nanotechnol.*, 15(2), 656–667 (2026). https://doi.org/10.13074/jent.2026.06.2622253

Suchitra, M. R., Bhuvaneswari, S. and Parthasarathy, S., Comparative Analysis of Phytochemical, Antioxidant, Antibacterial and Anticancer Activity of Musa acuminata Flower Florets and its Innermost Part Kuruthu, *J. Nat. Remedies*, 26(2), 531–539 (2026). https://doi.org/10.18311/jnr/2026/53214

Suresh, M., Karthikeyan, P. and Vadivel, P., Synthesis and Evaluation of Magnesium and Zinc-Doped Hydroxyapatite-Banana Flower Extract-PLGA Composite for Bone Regeneration, *Asia. J. Chem.*, 37(2), 465–472 (2025). https://doi.org/10.14233/ajchem.2025.33193

Tavassoli, M., Khezerlou, A., Sani, M. A., Hashemi, M., Firoozy, S., Ehsani, A., Khodaiyan, F., Adibi, S., Noori, S. M. A. and McClements, D. J., Methylcellulose/chitosan nanofiber-based composites doped with lactoferrin-loaded Ag-MOF nanoparticles for the preservation of fresh apple, *Int. J. Bio. Macromol.*, 259, 129182(2024). https://doi.org/10.1016/j.ijbiomac.2023.129182

Tiwari, A. V, Deshmukh, A. P., Tiwari, S. P., Dudhe, P. S., Yawale, D. S. and Yawale, S. P., Heterointerface-controlled charge modulation in Polypyrrole/TiO_2 nanocomposites for low-ppm CO_2 detection at room temperature, *Mater. Sci. Eng. B*, 332, 119670(2026). https://doi.org/10.1016/j.mseb.2026.119670

Tran, N. T., Le, T. N., Nguyen, L. M., Nguyen, G. T. and Ly, T. N., Broccoli leaf-derived carbon dots reinforced chitosan/gelatin film as UV-blocking, antioxidant, and antibacterial films for food packaging, *RSC Adv.*, 15(58), 50089–50102 (2025). https://doi.org/10.1039/d5ra07684f

Weiming, G., Quanfeng, H., Jianxia, S., Dan, L. and Xuejuan, D., Green synthesis of silver nanoparticles using banana flower extract, and their antibacterial activity, *Int. Food Res. J.*, 30(3), 613–625 (2023). https://doi.org/10.47836/ifrj.30.3.06

Yadav, V. K., Roy, S., Biswas, S., Dhara, S. and Pullela, M., Bioactive polyvinyl alcohol/chitosan films with novel streblus asper leaves- derived cellulose nanocrystals and Hygrophila auriculata oil for prolonging the shelf life of grapes: Machine learning modeling, and experimental approach, *Int. J. Bio. Macromol.*, 353, 151297(2026). https://doi.org/10.1016/j.ijbiomac.2026.151297

Zhou, W., Yu, J., Zhao, L., Wang, K., Hu, Z., Wu, J. Y. and Liu, X., Enhancement of chitosan-based film physicochemical and storage properties by interaction with proanthocyanidin and natural deep eutectic solvent, *Int. J. Bio. Macromol.*, 278, 134611(2024). https://doi.org/10.1016/j.ijbiomac.2024.134611